ACS APPLIED NANO MATERIALS

www.acsanm.org Article

Monte Carlo Simulations of Nanopore Compartmentalization Yield Fingerprint Adsorption Isotherms as a Rationale for Advanced Structure Characterization of Metal–Organic Frameworks

Shivam Parashar, Qing Zhu, Silvio Dantas, and Alexander V. Neimark*

Cite This: *ACS Appl. Nano Mater.* 2021, 4, 5531–5540 Read Online

ACCESS | Metrics & More | Article Recommendations | Supporting Information

ABSTRACT: Unique adsorption and transport properties of metal–organic framework (MOF) materials are determined by their complex nanostructures composed of three-dimensional (3D) networks of pore compartments (cages, channels, and windows) that differ in size, shape, and chemical functionalities. Practical MOF samples are rarely ideal crystals: they contain binders, various defects, and residual solvents. Reliable nanopore structure characterization methods are needed to quantify the difference between real samples and ideal MOF crystals. Here, we construct theoretical isotherms in the individual pore compartments of MOF crystals using Monte Carlo simulations and use them as reference fingerprint isotherms. The comparison of the experimental isotherms with the theoretical fingerprint isotherms allows one to calculate the pore type distribution function, degree of sample crystallinity, adsorption capacity, and accessibility of individual pore compartments. This information cannot be obtained with the currently available methods of adsorption characterization. The proposed methodology is demonstrated drawing on the examples of Ar, N_2, and CO_2 adsorption on porous coordination network-224 (PCN-224) and zeolitic imidazolate framework-412 (ZIF-412) MOF crystals. The constructed fingerprint isotherms are verified against the literature experimental data obtained by in situ adsorption crystallography. The pore-level compartmentalization of adsorption isotherms provides a better understanding of the specifics of the adsorption mechanisms and distribution of adsorbed molecules between the individual pore compartments, which is instrumental for the selection and design of adsorbents with improved properties for gas separation, storage, and catalysis.

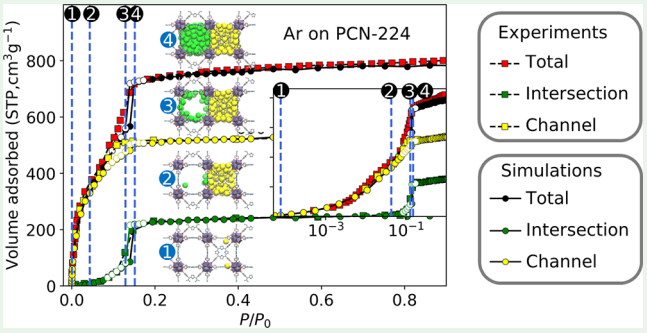

KEYWORDS: *metal–organic frameworks, adsorption isotherm, pore type distribution, density profile, monte carlo, pore structure characterization*

1. INTRODUCTION

Metal–organic frameworks (MOFs) represent a wide class of crystalline nanoporous materials that are actively explored for numerous applications because of their exceptional ability to selectively adsorb, transport, and retain guest molecules.[1−4] The unique abilities of MOFs stem from their tailorable porosity, record-high effective surface area, and extraordinary degree of the variability of active sites.[5,6] Significant progress has been made to understand the adsorption mechanisms[7−10] and develop advanced simulation techniques.[10−14] In case of ideal MOF crystals, the geometric properties of the crystallographic structure such as porosity, effective surface area, characteristic pore dimensions, and pore size distribution function can be determined using specially developed geometric methods, like Poreblazer,[15] and MOFomics.[16] The adsorption isotherms for the ideal MOF crystals can be predicted by Monte Carlo simulations using the standard force fields and software packages, like RASPA.[17] However, practical MOF samples are rarely ideal crystals, and they contain binders, secondary structures, various defects, and residual solvents; hence, their structural and adsorption properties may differ significantly from the properties of ideal crystals. It is important to devise pore structure methods to quantify the difference of the sample morphology from the ideal crystallographic structures in terms of the degree of crystallinity, available adsorption capacity, and accessibility of active centers.

Barrett–Joyner–Halenda (BJH) theory,[18] nonlocal density functional theory (NLDFT),[19] and quenched solid density functional theory (QSDFT)[20] are widely used methods to quantify the morphological properties of nanoporous materials in terms of pore size distribution (PSD). These methods fit the experimental adsorption isotherm to the kernel of theoretical

Received: April 5, 2021
Accepted: April 30, 2021
Published: May 13, 2021

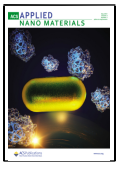

https://doi.org/10.1021/acsanm.1c00937
ACS Appl. Nano Mater. 2021, 4, 5531–5540

isotherms calculated in the model pores of simple shape (silt, cylindrical, or spherical) of different sizes. However, these conventional methods are unable to capture the specifics of the pore morphology of MOFs. MOF crystals possess a three-dimensional (3D) pore network composed of a regular array of interconnected pore compartments, channels, and cages that differ in size, shape, and chemistry. When applied to MOF materials, the conventional methods of pore structure characterization produce PSDs that are, in many cases, strikingly different compared to the geometric analysis of the respective crystallographic structures using the tools like Poreblazer[15] and MOFomics.[16] Characteristic examples of such discrepancies (presented in the Supporting Information Section F) demonstrate the need for developing dedicated characterization methods that consider the specifics of pore network morphologies in MOF materials.

The nonideality of practical MOF materials brings about additional complexity into the problem of pore structure characterization. All synthesized MOF samples contain defects to some extent. The defects may arise during the preparation method, imperfect activation of the sample, or sorption of contaminants during storage. The pores might be collapsed or blocked with nonvolatile molecules, binders, and residues. At the same time, the defects like missing linkers and nodes may produce larger pores and reduce diffusion limitations.[4] However, in general, the defects reduce the adsorption capacity and pore volume, reducing the pore space accessibility.[21] As a result, the experimental adsorption capacity is smaller compared to the ideal crystal capacity revealed in simulations. While comparing the simulated and experimental isotherms, it is common to introduce scaling factors to match the simulated capacity with experiments.[22] These scaling factors account for the inaccessible pores and nonporous inclusions without specifying their origin. It is worth noting that there were several attempts in the literature to account for the framework defects.[23,24] For example, Janabi et al.[23] considered Cu-benzene-1,3,5-tricarboxylate (Cu-BTC) MOF crystal and computed isotherms in several defective unit cells with blocked pockets, side pockets, and principal pore compartments. By comparing the simulated adsorption isotherms in defected pores with the experimental isotherms, the authors estimated the proportion of blocked pores.[23] Recently, Krause et al.[25] decomposed the methane isotherm to analyze the adsorption mechanisms in the Dresden University of Technology (DUT) family of MOFs exhibiting negative gas adsorption.

More recently, a new approach was suggested based on the decomposition or *compartmentalization* of adsorption isotherms as a sum of *fingerprint isotherms* in individual pore compartments. Applied to pore structure characterization from adsorption isotherms of reference molecular probes, the idea of compartmentalization is realized in the construction of the theoretical fingerprint isotherm using the molecular simulation of gas adsorption on the crystallographic structures of ideal MOF crystals.[8,24] The comparison of the measured isotherm of a MOF sample with a set of theoretical fingerprint isotherms allows one to construct the pore type distribution (PTD), which provides insights into the sample structure, such as the degree of crystallinity, available porosity, and accessibility of the pore compartments of various types. Moreover, the method of fingerprint isotherms was shown to correctly predict the isosteric heat of adsorption computed from the obtained PTD for the Cu-BTC sample, which is in agreement with the experimental data.[24]

In this work, we construct the theoretical fingerprint isotherms of Ar, N_2, and CO_2 in the pore compartments of porous coordination network-224 (PCN-224) and zeolitic imidazolate framework-412 (ZIF-412) MOF crystals. The choice of these systems is motivated by the availability of the experimental data presented in the pioneering study of Cho et al.,[26] who used the in situ X-ray diffraction (XRD) gas adsorption crystallography for the decomposition of adsorption isotherms into subisotherms in the individual pore compartments. This unique work provided, for the first time in the literature, the experimental data for the verification of the simulation results. The simulated fingerprint isotherms for all adsorbates considered are found in most cases, which is in excellent agreement with the experimental subisotherms.[26] Additional justification of the proposed simulation methodology is confirmed by comparing the density distributions of adsorbates between the pore compartments with the XRD crystallography data.[26] Finally, by comparing the experimental isotherms with the simulated fingerprint isotherms, the PCN-224 and ZIF-412 samples studied in ref[26] are characterized in terms of the PTD, revealing the degree of sample crystallinity, accessibility, and adsorption capacity of different pore compartments with respect to Ar, N_2, and CO_2.

2. METHODOLOGY

We performed Grand Canonical Monte Carlo (GCMC) simulations to obtain the adsorption isotherms using the open-source software package RASPA.[17] A minimum of 100,000 Monte Carlo moves were attempted for equilibration, and averages over at least 200,000 moves were performed for production. The probabilities for adsorbate translation, rotation, reinsertion, and swap moves were 0.2, 0.2, 0.2, and 0.4, respectively. All the isotherms were evaluated at the adsorbate normal boiling temperatures, that is, Ar (87.3 K), N_2 (77.4 K), and CO_2 (194.7 K). A simple Lennard-Jones (LJ) model was used for Ar,[27] whereas N_2 and CO_2 were modeled as rigid multicenter molecules described by the TraPPE[28] force field. The interaction parameters of the adsorbate with framework atoms were computed using Lorentz-Berthelot mixing rules. The LJ potentials for adsorbate interactions were truncated at 17 Å for Ar and N_2 and shifted at 12 and 15 Å for CO_2 in PCN-224 and ZIF-412, respectively. Polarization between the adsorbate and framework[11] was considered for CO_2 adsorption in PCN-224; the effect of CO_2 polarization on ZIF-412 was found to be negligible. Framework charges were obtained using the charge equilibration method,[29] and long-range electrostatic contributions were accounted using the Ewald summation method. The PCN-224 and ZIF-412 crystallographic structures were obtained from the previous literature.[30,31] The force-field parameters for the C, H, N, and O atoms were taken from Dreiding[32] force field, while Zr and Zn are from the UFF[33] force field (see Table S1 in the Supporting Information, Section A). The GCMC simulation cell of PCN-224 contains one cubic unit cell of size 38.512 × 38.512 × 38.512 nm^3 with 1216 framework atoms. From the atomic structure of PCN-224,[30] the central metal atom of the tetrakis (4-carboxyphenyl) porphyrin (TCPP) ring was removed to make our structure congruent to that in the experiments.[26] GCMC simulations in ZIF-412 were performed on the rhombohedral-shaped primitive unit cell, whose volume was one fourth of the cubic unit cell to reduce the

https://doi.org/10.1021/acsanm.1c00937
ACS Appl. Nano Mater. 2021, 4, 5531−5540

computational time. The size of the simulation cell was 51.056 × 51.056 × 51.056 nm^3 (α, β, γ = 60°,60°,60°) containing 3604 framework atoms. It is worth noting that some crystallographic sites in the ZIF-412 structure file[31] are partially occupied by multiple atoms because of an ambiguity in the distribution of some linkers: certain imidazole, benzimidazole, and nitro imidazole rings compete for the same sites (see Figure S11 in the Supporting Information). Multiple occupancies in the structure file represents a significant challenge as they must be removed in a non-ambiguous manner. We devised a special computational procedure to generate the structures with single occupancies of atomic sites by randomly assigning the competing groups to the sites in the given proportion (see the Supplementary Information, Section E).

3. RESULTS AND DISCUSSION

3.1. PCN-224. PCN-224 is composed of Zr_6O_8 clusters interlinked by tetrakis (4-carboxyphenyl)- porphyrin (TCPP) ligands.[30] Figure 1 shows the cubic unit cell of the PCN-224

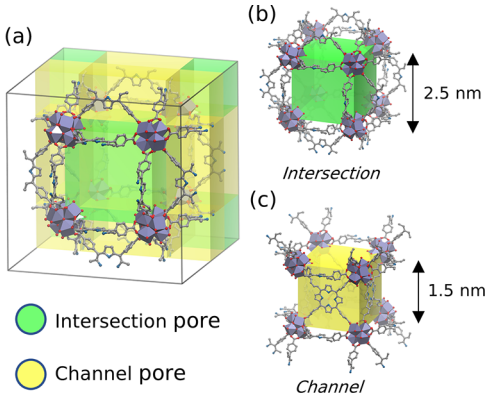

Figure 1. (a) Crystal structure of PCN-224 showing the division of unit cells into pore compartments. (b) Intersection and (c) channel pore. Framework atom color code: O, red; H, hidden; C, gray; N, blue; and Zr, violet.

crystal with two types of pores: intersection pores (green) located at the body center and vertices, and channel pores (yellow) located at the edges and face centers of the cubic unit cell. The channel and intersection pores of the nominal size of 1.5 and 2.5 nm[26] alternate on the cubic lattice with six channels and two intersection pores per unit cell. While the porphyrin walls block the channel pores from four out of six sides, the intersection pores are unobstructed on all the six sides. The unit cell was divided into compartments corresponding to the individual pores, as shown in Figure 1a. During the simulation run at a given pressure, the number of molecules in each compartment was averaged to construct the fingerprint isotherms (shown in Figure 2a).

The adsorption isotherm of argon on PCN-224 has two characteristic steps corresponding to each pore type, although the filling of each compartment occurs in a cooperative fashion (Figure 2). The channel pore (size ~1.5 nm) fills continuously at low pressures, which is typical for micropores. The filling step of the intersection pore (size ~2.5 nm) occurs stepwise via capillary condensation, as characteristic to mesopores. Figure 2b presents the snapshots of argon in each compartment at pressures indicated by vertical lines in Figure 2a. Argon molecules are colored according to the pores they reside in, that is, green for intersections and yellow for channels. The first (P/P_0 = 7.53 × 10^{-5}) and second (P/P_0 = 0.043) snapshots correspond to the onset of adsorption in the channel and intersection pores, respectively, whereas the third (P/P_0 = 0.129) and fourth (P/P_0 = 0.151) snapshots show the filled channel and intersection pores, respectively.

The simulated and experimental isotherms of Ar on PCN-224 are compared in Figure 3a. The simulated isotherms correspond to the ideal crystal with all pores completely accessible to the adsorbate. To match the simulated isotherms with the experimental data, we scale down the fingerprint isotherms in the channel and intersection pores by the accessibility factors of 0.58 and 0.62, respectively (Figure 3a). The scaled simulated isotherms are found to be in excellent agreement with the experiments in the whole range of gas pressure. This agreement suggests that the crystallinity of the PCN-224 sample used for the Ar measurements was ~60% or that the accessible pore volumes of the channel and intersection pores constituted ~58 and 62% of the respective pore volumes in the ideal crystal of the same weight as the sample.

Figure 3b, c presents the comparison between the total experimental and simulated isotherms of N_2 at 77.4 K and CO_2 at 194.7 K. Because the experimental subisotherms are not available for N_2 and CO_2, we scale the fingerprint isotherms to match the experimental density[26] at saturation for individual pores (indicated by the dashed lines). For N_2, the channel and intersection pore fingerprint isotherms are rescaled by 0.63 and 0.65, respectively. As expected, N_2 adsorption at 77 K (Figure 3a) occurs in a similar fashion as Ar at 87 K: the fingerprint isotherm for the intersection compartment exhibits a stepwise behavior, with pore filling occurring at ~0.15 P/P_0, while the channel pores are filled gradually. The total isotherm (black circles) represents the sum of the scaled fingerprint isotherm and agrees well with the experimental data (red squares) in the whole range of gas pressure.

The CO_2 isotherms on PCN-224 are presented in Figure 3c. We also included the polarization potential between the framework atoms and CO_2 molecules according to the previous literature.[11] Like the Ar and N_2 isotherms, we match the experimental adsorption capacities of individual pores (shown by dashed lines) by rescaling the CO_2 fingerprint isotherms in the channel and intersection pores by 0.66 and 0.70, respectively. CO_2 at 195 K fills the pores at higher pressures and in a broader range than Ar at 87 K and N_2 at 77 K because of the higher temperature of adsorption. Filling of the intersection pores with CO_2 starts when the channel pores are almost filled. The intersection pores are filled abruptly at P/P_0 = 0.42, and desorption occurs at lower pressures demonstrating a small H1-type hysteresis. It is worth noting that the polarization effects in PCN-224 are found to be very significant, especially at low pressures. The neglect of polarization leads to the underprediction of adsorption compared to the experiments (see the Supporting Information, Section A).

Adsorption and desorption isotherms simulated by GCMC commonly exhibit hysteresis in small mesopores of 2−4 nm, which is not observed in the experiments.[34−36] This behavior is found for CO_2 adsorption in the PCN-224 intersection pores of size ~2.5 nm. The adsorption hysteresis is related with the existence of the metastable states of confined fluid, which are separated from the equilibrium states by energy barriers. Because of limited simulation time and the absence of natural

https://doi.org/10.1021/acsanm.1c00937
ACS Appl. Nano Mater. 2021, 4, 5531−5540

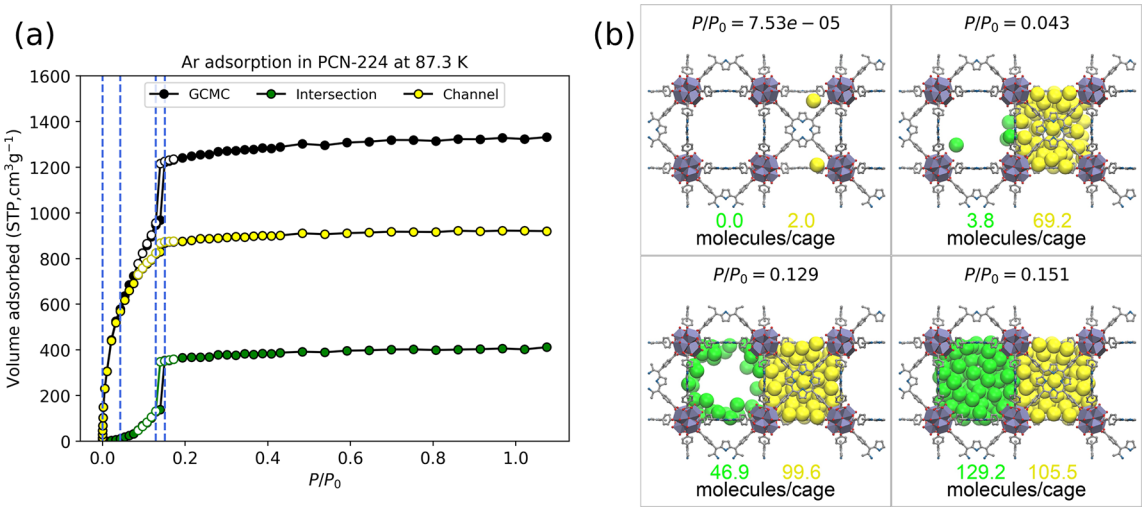

Figure 2. (a) Ar adsorption isotherm on PCN-224 obtained using the GCMC simulations at 87.3 K. Fingerprint isotherms in the intersection (green circles) and channel (yellow circles) pores are shown alongside the total isotherm (black circles). Closed and open circles correspond to adsorption and desorption isotherms, respectively. (b) Characteristic snapshots of the distribution of adsorbed molecules between the channel (green) and intersection (yellow) pores at different pressures from the onset of adsorption to the complete filling. Average number of molecules in each compartment is indicated below each snapshot. Vertical dashed lines in (a) indicate the pressures of the snapshots in (b). Framework atom color code: O, red; H, hidden; C, gray; N, blue; and Zr, violet.

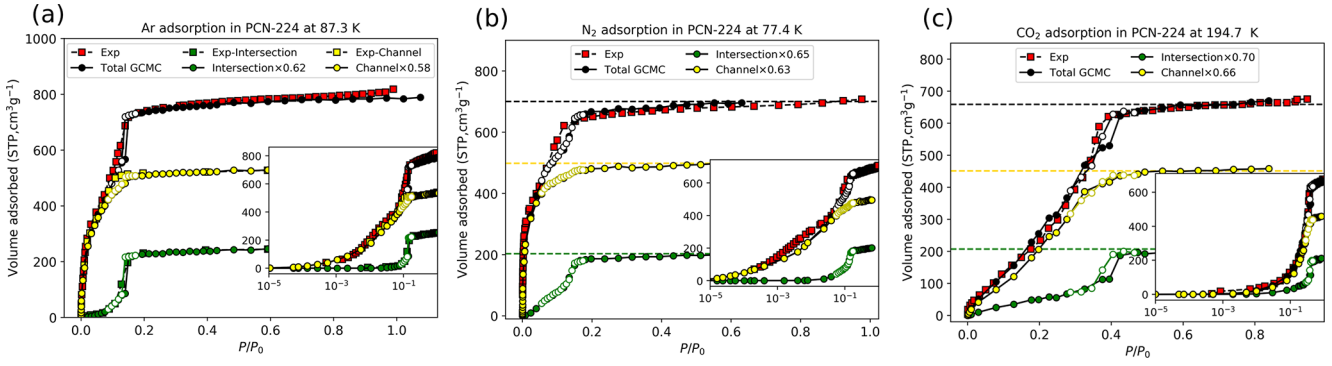

Figure 3. Comparison of the experimental[26] (squares) and simulated adsorption isotherms (circles) of (a) Ar at 87.3 K, (b) N_2 at 77.4 K, and (c) CO_2 at 194.7 K on PCN-224. The closed and open circles correspond to the adsorption and desorption isotherms. Fingerprint isotherms in the channel and intersection pores are plotted in yellow and green, respectively. (a) Simulated fingerprint isotherms are scaled down by the accessibility factors of 0.58 and 0.62 for the channel and intersection pore for Ar; (b) 0.63 and 0.65 for N_2; (c) 0.66 and 0.70 for CO_2 to match the experimental total capacity of each pore, which is indicated by the horizontal dashed lines.

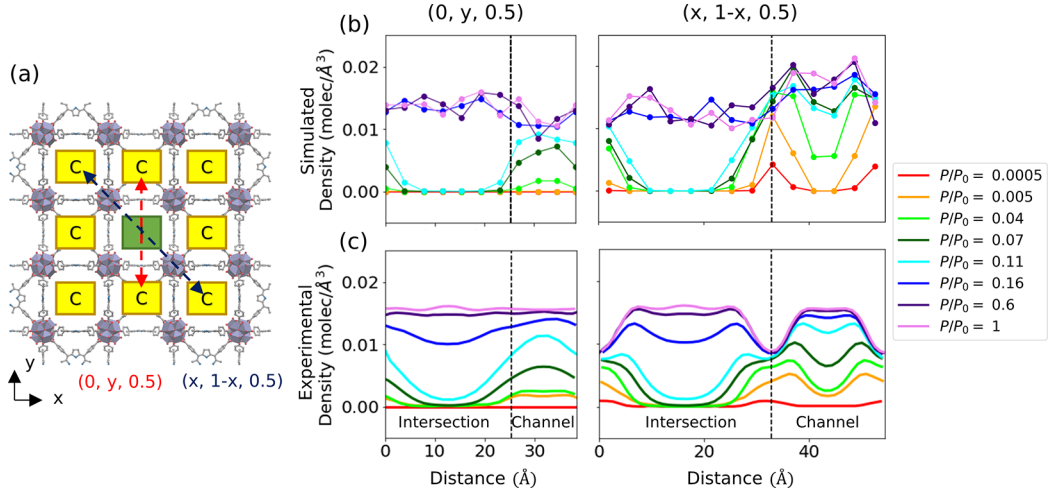

Figure 4. (a) Schematic of the PCN-224 unit cell showing the density profiles of argon along (0, y, 0.5) and (x, 1−x, 0.5) directions (b) simulated, and (c) experimental[26] density profiles. Simulated densities are multiplied by the factor of 0.7 to match the experimental densities.

https://doi.org/10.1021/acsanm.1c00937
ACS Appl. Nano Mater. 2021, 4, 5531−5540

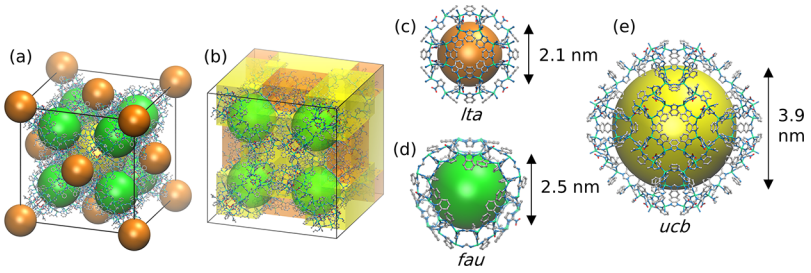

Figure 5. (a) Crystal structure of ZIF-412 showing the location of pores within a unit cell. (b) Division of the unit cell into pore compartments. (c), (d), (e) show the structure of lta, fau, and ucb cages, respectively, for which the pore volume is represented by a sphere. Framework atom color code; O: red, H: hidden, C: gray, N: blue, and Zn: green.

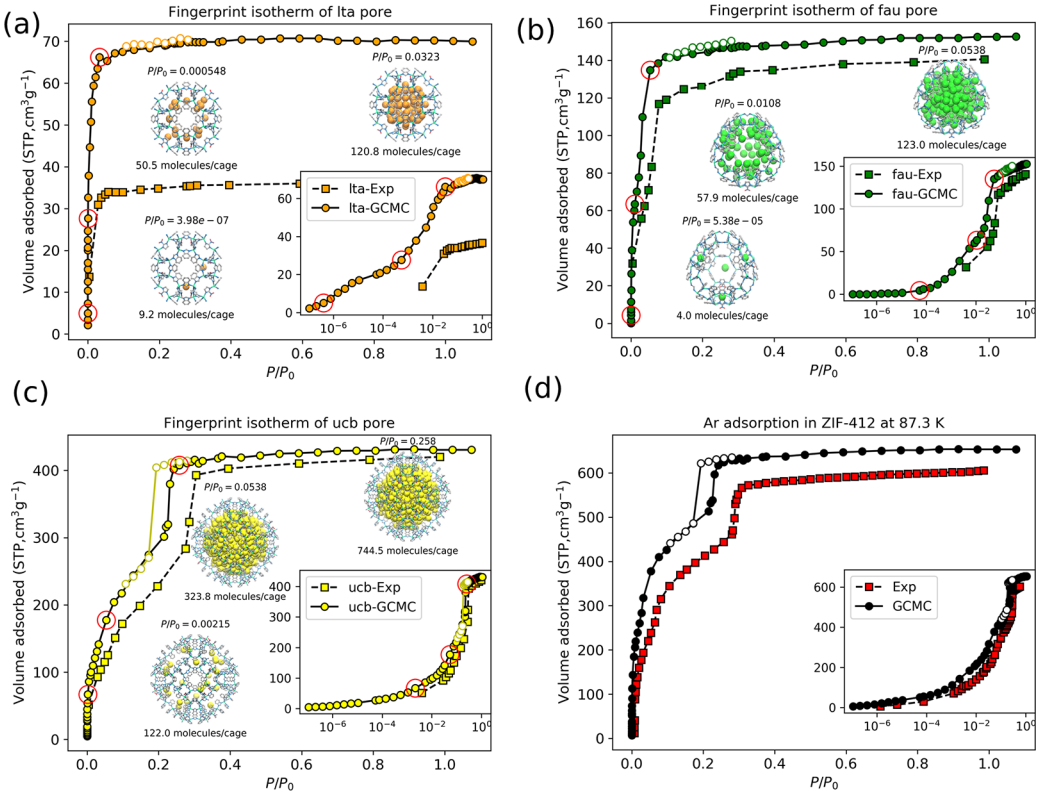

Figure 6. Comparison of the experimental (squares) and theoretical fingerprint isotherms (circles) of Ar in (a) lta, (b) fau, (c) ucb cage, and (d) total isotherms. The closed and open circles correspond to the adsorption and desorption isotherms, respectively. The red circles in the fingerprint isotherms correspond to the snapshots showing the sequence of adsorption. The average number of molecules adsorbed in each pore is printed below each snapshot.

fluctuations of external conditions, the probability of crossing the energy barriers in simulations is orders of magnitude smaller than that in the experiments. The larger the pore and the lower the temperature, the higher the energy barriers are. It was shown that in mesoporous materials, the adsorption hysteresis at normal boiling temperatures is observed experimentally only in pores larger than ∼4−5 nm, while in simulations, the hysteresis is inherent for pores larger than 2 nm.[36] Our simulations of adsorption in PCN-224 as well as in ZIF-412 confirm this conclusion.

Figure 4 shows the simulated and experimental density profiles of Ar in the channel and intersection pores at different pressures. The densities are presented along the lateral and diagonal directions. The simulated densities were scaled down by 0.7 to match the experimental density at saturation. The evolution of adsorbate densities as the pressure increases confirms that the channel pores are filled continuously. At P/P_0 = 0.11 (cyan), the intersection pore is empty while the channel pore is almost filled. A sudden increase in the density in the intersection pores from P/P_0 = 0.11 (cyan) to P/P_0 = 0.16 (blue) indicates the intersection pore filling due to capillary condensation. In the channel pores, the density along the lateral direction (x, 1−x, 0.5) is larger compared to that along the diagonal direction (0, y, 0.5) for the same pressure, which is due to the enhanced attractive potential created by the framework atoms along the diagonal direction. The simulated density profiles agree well with the experimental data. Such detailed agreement confirms the validity of our simulation methodology.

3.2. ZIF-412. The zeolitic imidazolate framework (ZIF)-412 framework is composed of Zn atoms bonded together with three types of linkers: imidazole, benzene imidazole, and nitro imidazole rings. ZIF-412 represents a mesoporous material with the pore network composed of three types of

https://doi.org/10.1021/acsanm.1c00937
ACS Appl. Nano Mater. 2021, 4, 5531−5540

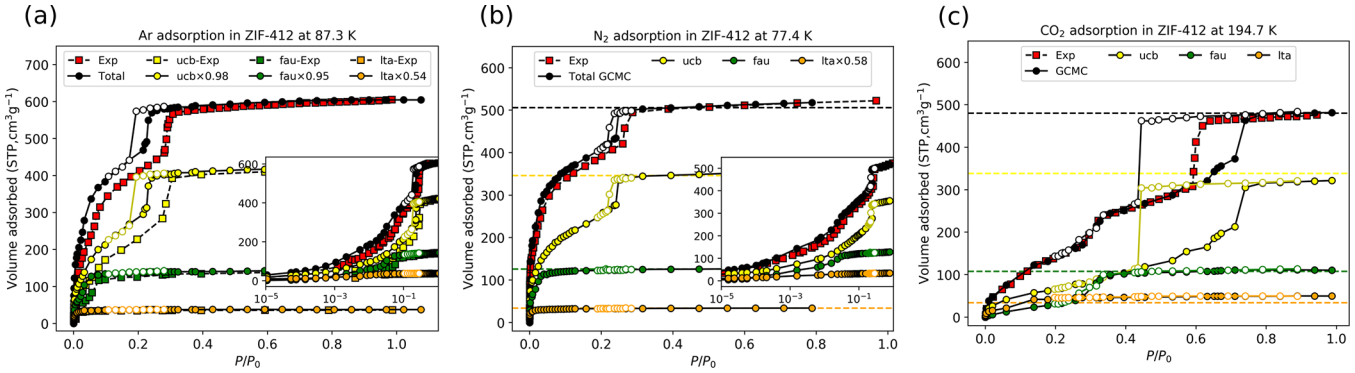

Figure 7. Comparison of the experimental[26] (squares) and simulated adsorption isotherms (circles) of (a) Ar at 87.3 K, (b) N_2 at 77.4 K, and (b) CO_2 at 194.7 K on ZIF-412. The open and closed circles correspond to the adsorption and desorption isotherms. For Ar, the accessibility factors for the lta, fau, and ucb cages are 0.54, 0.95, and 0.98, respectively, whereas for N_2, only the fingerprint isotherm in the lta cage is multiplied by the accessibility factor of 0.58 to match the experimental[26] pore capacities (horizontal dashed lines). For CO_2, all the accessibility factors are equal to 1.

cagelike compartments connected by narrower windows. Figure 5a shows the pore arrangement in the cubic unit cell of the ZIF-412 crystal: lta (Linde Type A) cages in orange are located on the face centers and vertices, fau (Faujasite) cages in green are located on the cube diagonals close to the vertices, and ucb[31] cages (yellow) are located at the unit cell center and the edges (latter is not shown for the sake of clarity). The lta pore is the smallest of the three pores with the geometric diameter of 2.1 nm. Six narrow 0.8 nm windows connect the lta pores to the ucb cages of size 3.9 nm. Each ucb cage is connected to eight fau cages of size 2.5 nm. The pore window between ucb and fau cages is 1.5 nm wide. We divide the unit cell into the pore compartments (Figure 5b) and count the average number of molecules in each compartment to construct the fingerprint isotherm.

The simulated Ar isotherms on ZIF-412 are shown in Figure 6 in comparison with the experimental data.[26] The GCMC isotherm in Figure 6d has a H1-type hysteresis loop typical for capillary condensation in mesoporous solids. However, the shape of the isotherm prior to the condensation transition is more convex compared to the multilayer adsorption isotherm usually observed for mesoporous materials. The experimental isotherm has a similar shape as the simulated isotherm with three main distinctions. First, the experimental isotherm is reversible that is common for mesoporous materials with pores smaller than 4 nm; the absence of hysteresis is explained by the low nucleation barriers of capillary condensation that can be overcome because of natural thermal fluctuations in the experiments but are prohibitive in MC simulations.[35] Second, experimental capillary condensation takes place at a higher vapor pressure than that in MC simulations. This discrepancy could not be improved by the force-field adjustment within reasonable limits. Possible reasons for this discrepancy are discussed in the Supplementary Information, Sections B and C. In particular, we show that the increase of simulation temperature to 90 K gives good correspondence with the experiments. Third, the experimental adsorption capacity is ~90% of the simulations indicating that either the sample has nonporous inclusions or a significant portion of pores is blocked and inaccessible. The answer to this question is revealed by the analysis of the fingerprint isotherms.

The fingerprint isotherms shed light on the specifics of the adsorption mechanisms because of the morphological complexity of the ZIF-412 pore structure comprising three distinct pore compartments. The fingerprint isotherms of Ar adsorption in the lta, fau, and ucb cages are shown in Figure 6a–c. We observe that the lta pores are gradually filled, achieving the complete capacity at ~0.03 P/P_0. The filling of the fau cages is associated with a sharper reversible step between ~0.01–0.05 P/P_0. In contrast, adsorption in the ucb cages exhibits a capillary condensation–desorption hysteresis loop at ~0.18–0.26 P/P_0. The simulated isotherms correspond to the ideal crystal with all the pores fully accessible because of which the fingerprint isotherms (circles) predict larger adsorption compared to the experimental subisotherms. It is worth noting that the subisotherms[26] are determined from the XRD measurements; they start from higher pressures ($P/P_0 \sim 10^{-2}$) and contain fewer points than the total isotherm measured volumetrically. The lta fingerprint isotherms have the largest difference in the saturation capacity compared to the experimental subisotherms (Figure 6a). This suggests that a significant portion of the lta pores is inaccessible in the experimentally studied crystal. Indeed, as seen in Figure 7a, scaling down the lta fingerprint isotherm by the accessibility factor of 0.54 results in a good match with the experimental subisotherm determined by in situ XRD crystallography. At the same time, the theoretical adsorption capacities of the fau and ucb cages are close to the experimental capacities that suggest a minor blockage of these pore compartments. To match the experimental data, the fingerprint isotherms of the fau and ucb cages were scaled down by the accessibility factors of 0.95 and 0.98, respectively (Figure 7a).

Figure 7b, c presents the comparison between the total simulated and experimental isotherms of N_2 at 77.4 K and CO_2 at 194.7 K. For N_2, the accessibility factors are 0.58, 1, and 1 for the lta, fau, and ucb pores, respectively, indicating that only 58% of the lta pores were accessible in the experimentally studied samples, whereas all the fau and ucb pores were fully accessible. The total isotherm (black circles) is the sum of the scaled fingerprint isotherm which agrees well with the experimental data (red squares). The overall pore filling behavior of N_2 at 77 K is very similar to the Ar adsorption:filling in lta pores below ~0.02 P/P_0, in fau pores at pressure below ~0.03 P/P_0, and in ucb pores at slightly higher relative pressures of ~0.22–0.25. N_2 also exhibits a hysteresis, but it is smaller compared to Ar (Figure 7a).

For CO_2 (Figure 7b), the accessibility factors for the lta, fau, and ucb cages are equal to one, suggesting that all the pores are completely accessible to CO_2 in the experimental sample. This may be due to its smaller kinetic diameter and higher

https://doi.org/10.1021/acsanm.1c00937
ACS Appl. Nano Mater. 2021, 4, 5531–5540

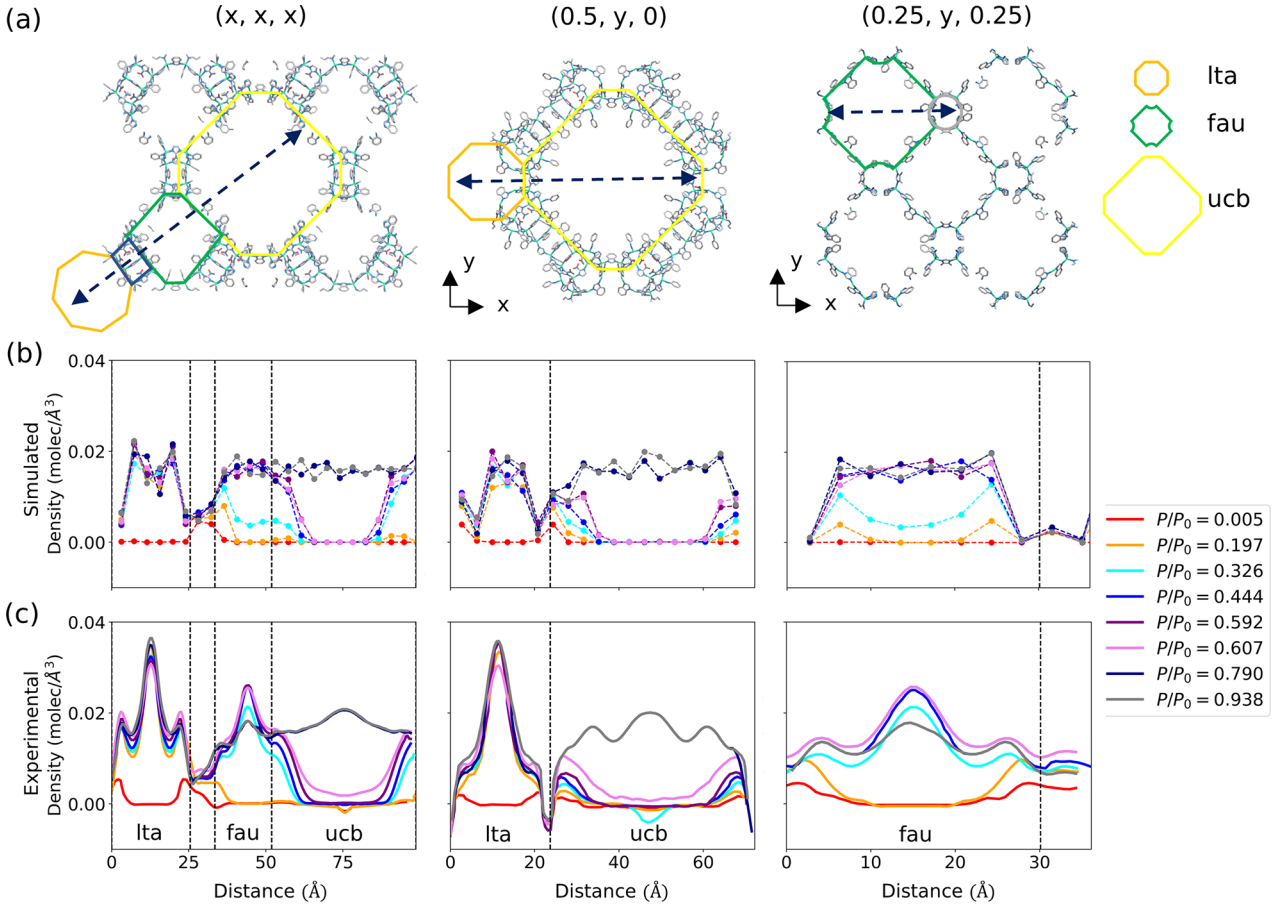

Figure 8. (a) Schematic of the ZIF-412 structure showing the directions (x, x, x), (0.5, y, 0), and (0.25, y, 0.25), along which the density profile of CO_2 was computed at various pressures. (b) Simulated and (c) experimental[26] density profiles in each of those directions.

temperature (194.7 K) compared to Ar (87.3 K) and N_2 (77.4 K). The agreement between the total simulated and experimental isotherms is accurate, except that the simulated isotherms exhibit a wide hysteresis in the ucb cage whereas experimental isotherm is reversible. The hysteresis loop is widest for CO_2 in comparison to Ar and N_2 because the adsorption temperature of CO_2 (194.7 K) is well below the triple point (216.6 K). The hysteretic behavior in our simulations is due to the formation of a metastable state and lower thermal fluctuations, which would disappear for an infinitely long simulation.[37,38]

We computed the density profiles of CO_2 along three directions connecting the lta, fau, and ucb pores diagonally, the lta and ucb cages laterally, and two fau cages laterally, as shown in Figure 8a. The simulated density profiles (Figure 8b) confirm that the lta pore gets filled before P/P_0~0.197 (orange), fau between P/P_0~0.326−0.444, and ucb below P/P_0~0.790. Compared to the experimental density profile (Figure 8c), the simulated profiles are in good qualitative and quantitative agreement.

3.3. Pore Type Distribution (PTD). The fingerprint isotherms allow for the analysis of the extent to which the pore structure of a given MOF sample is similar (or different) to the pore structure of the ideal crystal and the calculation of the PTD. To this end, the experimental isotherm, N_{exp}, is presented as a weighed sum of the fingerprint isotherms, N_i^{FP},

$$N_{exp} = \sum_i \varphi_i N_i^{FP} \quad (1)$$

The weights φ_i represent the contributions of the individual pore compartments into the total adsorption and represent the accessibility factors, which quantify the deviations of the sample structure from the ideal crystal.

For the PCN-224 and ZIF-412 samples considered here, the PTD is presented as the histogram of the volumes of individual pores accessible for the given adsorbate per unit mass of the sample (Figure 9). Here, the pore volumes are defined not from their geometry in the crystallographic structure but from the adsorption capacities using the Gurvich rule[39] by dividing the adsorption at saturation ($P/P_0 \rightarrow 1$) in mol/g by the bulk fluid density in cc/mol.[40] This is why the pore volumes determined using different adsorbates may differ. The accessibility factors φ_i characterize the ratio of the accessible volume of the given pore compartment in the sample to the compartment volume in the ideal crystal. The hollow transparent bars shown in Figure 9 represent the pore volumes of the individual pores accessible for Ar, N_2, and CO_2 in the ideal crystal, and the filled bars represent the respective pore volumes determined from the experimental isotherms. The percentage (φ_i*100%) of pore volume available in the experiments compared to the ideal volume available in simulations is indicated on each bar.

For the PCN-224 sample (Figure 9a), the channel and intersection pores are almost equally available: ~60% for argon adsorption, ~64% for N_2, and ~68% for CO_2. This suggests that the crystallinity of the sample (in terms of the ratio of the mass of the crystal phase to the sample mass) is about ~64

https://doi.org/10.1021/acsanm.1c00937
ACS Appl. Nano Mater. 2021, 4, 5531−5540

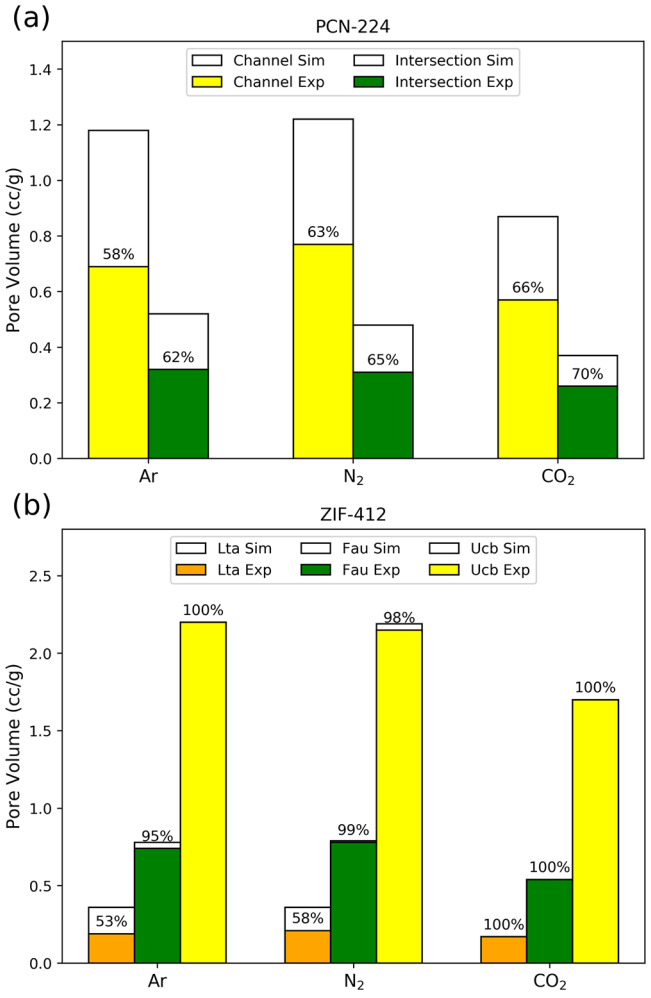

Figure 9. Pore type distibution (PTD) in (a) PCN-224 and (b) ZIF-412 calculated for Ar, N_2, and CO_2. The empty bars represent the simulated pore volume of each pore type while the filled colored bars are experimental pore volumes. The accessibility factors (in percentage) are printed on the top of the bars.

+/−4%. For the ZIF-412 sample (Figure 9b), CO_2 adsorption indicates that the sample is close to the ideal crystal, as the experimental accessibility of all the three pore compartments is ∼100%. However, while the fau and ucb cages are also almost fully accessible for Ar and N_2, the smallest lta pores are only partially accessible (∼53 and ∼58%) by these adsorbates. The explanation why the lta pores are fully accessible for CO_2 but only partially accessible for Ar and N_2 deserve further analysis of the specifics of the ZIF-412 structure. For both the MOF samples, the volume accessed by different adsorbates follows this order: CO_2 > N_2 > Ar. CO_2 accessed all the pores in ZIF-412 because of its smaller kinetic diameter and higher adsorption temperature of CO_2 (194.7 K) compared to argon (87.3 K) and N_2 (77.4 K).

In the above analysis of PTD in the PCN-224 and ZIF-412 samples, we took advantage of the availability of the experimental subisotherms in individual pore compartments. PTD can be determined based on the standard measurements of the total adsorption isotherm by fitting the accessibility factors φ_i of the simulated fingerprint isotherms, N_i^{FP}, in eq 1 to reproduce the experimental isotherm, N_{exp}.

4. CONCLUSIONS

To what extent are the nanopore structures of the synthesized samples of MOF materials are different from the ideal crystals? This is an important question for the design and selection of novel MOF structures for practical applications. The samples of MOF materials rarely represent ideal crystals and, in most cases, contain noncrystalline inclusions like binders, residual chemicals, and various types of defects. The cages and channels of varied sizes, shapes, and chemistries, which comprise the three-dimensional pore network, may be completely or partially blocked, thus reducing the pore accessibility and adsorption capacity. The method of fingerprint isotherms, proposed by us recently,[24] allows to assess the degree of sample crystallinity, adsorption capacities, and accessibilities of different pore compartments from the experimental adsorption isotherms. The method is based on the construction by MC simulations, the theoretical adsorption isotherm that is divided into a set of reference fingerprint isotherms corresponding to the individual pore compartments of the ideal crystallographic structure. The pore accessibilities are calculated as the weights in the representation of the experimental isotherm as a weighted sum of fingerprint isotherms. The results are presented in terms of the PTD that determines the accessible volume fractions of the pores of different types in the sample under study.

The method of fingerprint isotherms is illustrated and validated drawing on the examples of the adsorption of Ar, N_2, and CO_2 adsorption at the respective normal boiling temperatures on the PCN-224 and ZIF-412 MOF materials. This choice is motivated by the availability of the unique data of in situ adsorption XRD crystallography that for the first time allowed for the identification of measured adsorption in different pore compartments, construction of respective subisotherms, and 3D adsorbate density distribution in the pore system at varying gas pressures.[26] We found good agreement between the simulated and experimental data not only on the isotherms measured crystallographically and volumetrically but also on the adsorbate density profiles in different crystallographic directions. The latter comparison is most instructive and reveals the detailed adsorption and pore filling mechanisms. The calculated PTD and accessibility factors made it possible to make conclusions about the quality of the samples considered. By comparing the fingerprint isotherms with the experiments, one evaluates the accessibility factors of individual pore compartments for a given adsorbate. The accessibility factors depend on the degree of crystallinity (fraction of crystalline phase in the sample) and on the compartment accessibilities within the crystal. The degree of crystallinity may be determined by an expert estimate, as the largest accessibility factor among all pore compartments for a given adsorbate. In case of ZIF-412, the degree of crystallinity is ∼100% with the ucb and fau pores fully available to all adsorbates and the lta pores fully available for CO_2 and only partially for Ar and N_2. In case of PCN-224, the accessibility factors vary between 58 and 70%, and it is safe to conclude the crystallinity factor of not larger than 70%, assuming that the channel pores in the crystalline phase are fully available to CO_2. These examples show that the method of fingerprint isotherms provides a better understanding of the specifics of the adsorption mechanisms and distribution of adsorbed molecules between the individual nanopore compartments that is instrumental for the selection and design of novel adsorbents

https://doi.org/10.1021/acsanm.1c00937
ACS Appl. Nano Mater. 2021, 4, 5531−5540

with improved properties for gas separations, storage, and catalysis.

Our calculations confirm the importance of the polarization effect for CO_2 adsorption on MOFs. The difference between the simulations with and without the polarization potential between CO_2 and the PCN-224 framework is found to be very significant (see Figure S1). The neglect of the polarization effect causes a shift of the adsorption isotherms to higher pressures compared with the experimental isotherm. At the same time, the polarization effect for CO_2 adsorption on ZIF-412 is found to be insignificant.

The method of fingerprint isotherms can be extended to other families of MOF materials, as the crystallographic structures are available in different databases[41,42] and theoretical fingerprint isotherms can be calculated using standard forcefields (UFF, Dreiding, etc.) with the MC simulation software package like RASPA.[17] However, while the MC simulation of adsorption isotherms is considered as a routine, there are certain challenges that must be critically evaluated and analyzed. Some of these issues, that we encountered in the systems studied here, are discussed in the text and in the Supplementary Information. The division of the pore space into individual pore compartments, that is in many systems obvious, for some structures may be ambiguous because of the pore intersections that can be attributed to either of the neighboring pores. MOFs with different types of linkers, such as ZIF-412, can contain fractional occupancies in their crystallographic structures and must be treated prior to adsorption modeling. For the adjustment of structures with fractional occupancies, we devised a computational procedure that can be adopted for other structures (see Supporting Information, section E). It is very important to visualize the structure carefully (to check for partial occupancies of atoms) and clean it before performing GCMC simulations. The removal of partial occupancies using our algorithm gives not one but a collection of true structures that differ in the relative positioning of the linkers. Another important complication arises from different degrees of hydration and nonuniform distribution of residual chemicals in practical samples that not only alter the adsorption space and pore dimensions but also affect the adsorption interactions. It is worth noting that as shown in the presented examples, the pore structure characteristics determined from the adsorption of different adsorbates may differ. In this respect, CO_2 has certain advantages as a molecular probe compared to N_2 and Ar because of its higher mobility and capability of penetrating into the smallest micropores.

The proposed methodology can be extended further to evaluate the nanopores within the secondary binder phase and defected pores within the crystal phase of MOF materials by combining the kernel of fingerprint isotherms with a conventional kernel of theoretical isotherms obtained using the NLDFT or QSDFT methods.[43] Such hybrid kernels will allow for the determination of the accessibilities of intact pore compartments in the crystal phase and the effective size distribution of the binder and defective pores.

■ ASSOCIATED CONTENT

Supporting Information

The Supporting Information is available free of charge at https://pubs.acs.org/doi/10.1021/acsanm.1c00937.

Supporting Information with simulation details, density profile calculations, dependence of isotherms on the truncation of potential, pore volumes, and partial occupancies in ZIF-412 (PDF).

■ AUTHOR INFORMATION

Corresponding Author

Alexander V. Neimark − *Department of Chemical and Biochemical Engineering, Rutgers, The State University of New Jersey, Piscataway, New Jersey 08854, United States;* orcid.org/0000-0002-3443-0389; Email: aneimark@rutgers.edu

Authors

Shivam Parashar − *Department of Chemical and Biochemical Engineering, Rutgers, The State University of New Jersey, Piscataway, New Jersey 08854, United States;* orcid.org/0000-0002-0323-7391

Qing Zhu − *Department of Physics, Applied Physics, Astronomy - Rensselaer Polytechnic Institute, Troy, New York 12180, United States; Department of Chemical and Biochemical Engineering, Rutgers, The State University of New Jersey, Piscataway, New Jersey 08854, United States*

Silvio Dantas − *Department of Chemical and Biochemical Engineering, Rutgers, The State University of New Jersey, Piscataway, New Jersey 08854, United States;* orcid.org/0000-0001-7168-4938

Complete contact information is available at: https://pubs.acs.org/10.1021/acsanm.1c00937

Author Contributions

All authors have given approval to the final version of the manuscript.

Funding

This work is supported by the National Science Foundation (CBET grant no. 1834339).

Notes

The authors declare no competing financial interest.

■ ACKNOWLEDGMENTS

The author expresses a huge thanks to Filip Formalik and Peter Ravikovitch for useful discussions.

■ REFERENCES

(1) Zhou, H.-C.; Long, J. R.; Yaghi, O. M. Introduction to Metal−Organic Frameworks. *Chem. Rev.* **2012**, *112*, 673−674.

(2) Pascanu, V.; González Miera, G.; Inge, A. K.; Martín-Matute, B. Metal-Organic Frameworks as Catalysts for Organic Synthesis: A Critical Perspective. *J. Am. Chem. Soc.* **2019**, *141*, 7223−7234.

(3) Sturluson, A.; Huynh, M. T.; Kaija, A. R.; Laird, C.; Yoon, S.; Hou, F.; Feng, Z. X.; Wilmer, C. E.; Colon, Y. J.; Chung, Y. G.; Siderius, D. W.; Simon, C. M. The role of molecular modelling and simulation in the discovery and deployment of metal-organic frameworks for gas storage and separation(dagger). *Mol. Simul.* **2019**, *45*, 1082−1121.

(4) Xiang, W.; Zhang, Y.; Chen, Y.; Liu, C.-J.; Tu, X. Synthesis, characterization and application of defective metal−organic frameworks: current status and perspectives. *J. Mater. Chem. A* **2020**, *8*, 21526−21546.

(5) Cohen, S. M. Postsynthetic Methods for the Functionalization of Metal−Organic Frameworks. *Chem. Rev.* **2012**, *112*, 970−1000.

(6) Yuan, S.; Feng, L.; Wang, K.; Pang, J.; Bosch, M.; Lollar, C.; Sun, Y.; Qin, J.; Yang, X.; Zhang, P.; Wang, Q.; Zou, L.; Zhang, Y.; Zhang, L.; Fang, Y.; Li, J.; Zhou, H.-C. Stable Metal-Organic Frameworks:

Design, Synthesis, and Applications. *Adv. Mater.* **2018**, *30*, No. 1704303.
(7) Cychosz Struckhoff, K.; Thommes, M.; Sarkisov, L. On the Universality of Capillary Condensation and Adsorption Hysteresis Phenomena in Ordered and Crystalline Mesoporous Materials. *Adv. Mater. Interfaces* **2020**, *7*, No. 2000184.
(8) Dantas, S.; Sarkisov, L.; Neimark, A. V. Deciphering the Relations between Pore Structure and Adsorption Behavior in Metal−Organic Frameworks: Unexpected Lessons from Argon Adsorption on Copper−Benzene-1,3,5-tricarboxylate. *J. Am. Chem. Soc.* **2019**, *141*, 8397−8401.
(9) Park, J.; Howe, J. D.; Sholl, D. S. How Reproducible Are Isotherm Measurements in Metal−Organic Frameworks? *Chem. Mater.* **2017**, *29*, 10487−10495.
(10) Walton, K. S.; Millward, A. R.; Dubbeldam, D.; Frost, H.; Low, J. J.; Yaghi, O. M.; Snurr, R. Q. Understanding inflections and steps in carbon dioxide adsorption isotherms in metal-organic frameworks. *J. Am. Chem. Soc.* **2008**, *130*, 406−407.
(11) Becker, T. M.; Dubbeldam, D.; Lin, L.-C.; Vlugt, T. J. H. Investigating polarization effects of CO2 adsorption in MgMOF-74. *J. Comput. Sci.* **2016**, *15*, 86−94.
(12) Jablonka, K. M.; Ongari, D.; Smit, B. Applicability of Tail Corrections in the Molecular Simulations of Porous Materials. *J. Chem. Theory Comput.* **2019**, *15*, 5635−5641.
(13) Ongari, D.; Boyd, P. G.; Kadioglu, O.; Mace, A. K.; Keskin, S.; Smit, B. Evaluating Charge Equilibration Methods To Generate Electrostatic Fields in Nanoporous Materials. *J. Chem. Theory Comput.* **2019**, *15*, 382−401.
(14) Zhang, K.; Nalaparaju, A.; Chen, Y.; Jiang, J. Crucial role of blocking inaccessible cages in the simulation of gas adsorption in a paddle-wheel metal-organic framework. *RSC Adv.* **2013**, *3*, 16152−16158.
(15) Sarkisov, L.; Harrison, A. Computational structure characterisation tools in application to ordered and disordered porous materials. *Mol. Simul.* **2011**, *37*, 1248−1257.
(16) First, E. L.; Floudas, C. A. MOFomics: Computational pore characterization of metal-organic frameworks. *Microporous Mesoporous Mater.* **2013**, *165*, 32−39.
(17) Dubbeldam, D.; Calero, S.; Ellis, D. E.; Snurr, R. Q. RASPA: Molecular simulation software for adsorption and diffusion in flexible nanoporous materials. *Mol. Simul.* **2016**, *42*, 81−101.
(18) Barrett, E. P.; Joyner, L. G.; Halenda, P. P. The Determination of Pore Volume and Area Distributions in Porous Substances. I. Computations from Nitrogen Isotherms. *J. Am. Chem. Soc.* **1951**, *73*, 373−380.
(19) Lastoskie, C.; Gubbins, K. E.; Quirke, N. Pore size distribution analysis of microporous carbons: a density functional theory approach. *J. Phys. Chem.* **1993**, *97*, 4786−4796.
(20) Ravikovitch, P. I.; Neimark, A. V. Density Functional Theory Model of Adsorption on Amorphous and Microporous Silica Materials. *Langmuir* **2006**, *22*, 11171−11179.
(21) Moellmer, J.; Celer, E. B.; Luebke, R.; Cairns, A. J.; Staudt, R.; Eddaoudi, M.; Thommes, M. Insights on Adsorption Characterization of Metal-Organic Frameworks: A Benchmark Study on the Novel soc-MOF. *Microporous Mesoporous Mater.* **2010**, *129*, 345−353.
(22) Chowdhury, P.; Bikkina, C.; Meister, D.; Dreisbach, F.; Gumma, S. Comparison of adsorption isotherms on Cu-BTC metal organic frameworks synthesized from different routes. *Microporous Mesoporous Mater.* **2009**, *117*, 406−413.
(23) Al-Janabi, N.; Fan, X.; Siperstein, F. R. Assessment of MOF's Quality: Quantifying Defect Content in Crystalline Porous Materials. *J. Phys. Chem. Lett.* **2016**, *7*, 1490−1494.
(24) Dantas, S.; Neimark, A. V. Coupling Structural and Adsorption Properties of Metal-Organic Frameworks: From Pore Size Distribution to Pore Type Distribution. *ACS Appl. Mater. Interfaces* **2020**, *12*, 15595−15605.
(25) Krause, S.; Evans, J. D.; Bon, V.; Senkovska, I.; Iacomi, P.; Kolbe, F.; Ehrling, S.; Troschke, E.; Getzschmann, J.; Többens, D. M.; Franz, A.; Wallacher, D.; Yot, P. G.; Maurin, G.; Brunner, E.; Llewellyn, P. L.; Coudert, F.-X.; Kaskel, S. Towards general network architecture design criteria for negative gas adsorption transitions in ultraporous frameworks. *Nat. Commun.* **2019**, *10*, 3632.
(26) Cho, H. S.; Yang, J.; Gong, X.; Zhang, Y. B.; Momma, K.; Weckhuysen, B. M.; Deng, H.; Kang, J. K.; Yaghi, O. M.; Terasaki, O. Isotherms of individual pores by gas adsorption crystallography. *Nat. Chem.* **2019**, *11*, 562−570.
(27) Rowley, L. A.; Nicholson, D.; Parsonage, N. G. Monte Carlo grand canonical ensemble calculation in a gas-liquid transition region for 12-6 Argon. *J. Comput. Phys.* **1975**, *17*, 401−414.
(28) Potoff, J. J.; Siepmann, J. I. Vapor−liquid equilibria of mixtures containing alkanes, carbon dioxide, and nitrogen. *AIChE J.* **2001**, *47*, 1676−1682.
(29) Rappe, A. K.; Goddard, W. A., III Charge equilibration for molecular dynamics simulations. *J. Phys. Chem.* **1991**, *95*, 3358−3363.
(30) Feng, D.; Chung, W. C.; Wei, Z.; Gu, Z. Y.; Jiang, H. L.; Chen, Y. P.; Darensbourg, D. J.; Zhou, H. C. Construction of ultrastable porphyrin Zr metal-organic frameworks through linker elimination. *J. Am. Chem. Soc.* **2013**, *135*, 17105−17110.
(31) Yang, J.; Zhang, Y. B.; Liu, Q.; Trickett, C. A.; Gutierrez-Puebla, E.; Monge, M. A.; Cong, H.; Aldossary, A.; Deng, H.; Yaghi, O. M. Principles of Designing Extra-Large Pore Openings and Cages in Zeolitic Imidazolate Frameworks. *J. Am. Chem. Soc.* **2017**, *139*, 6448−6455.
(32) Mayo, S. L.; Olafson, B. D.; Goddard, W. A. Dreiding - a Generic Force-Field for Molecular Simulations. *J. Phys. Chem.* **1990**, *94*, 8897−8909.
(33) Rappe, A. K.; Casewit, C. J.; Colwell, K. S.; Goddard, W. A., III; Skiff, W. M. Uff, a Full Periodic-Table Force-Field for Molecular Mechanics and Molecular-Dynamics Simulations. *J. Am. Chem. Soc.* **1992**, *114*, 10024−10035.
(34) Dantas, S.; Struckhoff, K. C.; Thommes, M.; Neimark, A. V. Phase Behavior and Capillary Condensation Hysteresis of Carbon Dioxide in Mesopores. *Langmuir* **2019**, *35*, 11291−11298.
(35) Neimark, A. V.; Vishnyakov, A. Phase Transitions and Criticality in Small Systems: Vapor−Liquid Transition in Nanoscale Spherical Cavities. *J. Phys. Chem. B* **2006**, *110*, 9403−9412.
(36) Neimark, A. V.; Ravikovitch, P. I.; Vishnyakov, A. Adsorption hysteresis in nanopores. *Phys. Rev. E Stat. Phys. Plasmas. Fluids Relat. Interdiscip. Topics* **2000**, *62*, R1493−R1496.
(37) Schoen, M.; Rhykerd, C. L., Jr.; Cushman, J. H.; Diestler, D. J. Slit-pore sorption isotherms by the grand-canonical Monte Carlo method. *Mol. Phys.* **2006**, *66*, 1171−1182.
(38) Sarkisov, L.; Monson, P. A. Hysteresis in Monte Carlo and Molecular Dynamics Simulations of Adsorption in Porous Materials. *Langmuir* **2000**, *16*, 9857−9860.
(39) Rouquerol, F.; Rouquerol, J.; Sing, K., Assessment of Mesoporosity. In *Adsorption by Powders and Porous Solids*, Rouquerol, F.; Rouquerol, J.; Sing, K., Eds. Academic Press: London, 1999; 191−217.
(40) Lemmon, E. W.; McLinden, M. O.; Friend, D. G., Thermophysical Properties of Fluid Systems. In *NIST Chemistry WebBook, NIST Standard Reference Database Number 69*, Eds. P.J., Linstrom; W.G., Mallard, National Institute of Standards and Technology, Gaithersburg MD, 20899.
(41) Chung, Y. G.; Camp, J.; Haranczyk, M.; Sikora, B. J.; Bury, W.; Krungleviciute, V.; Yildirim, T.; Farha, O. K.; Sholl, D. S.; Snurr, R. Q. Computation-Ready, Experimental Metal−Organic Frameworks: A Tool To Enable High-Throughput Screening of Nanoporous Crystals. *Chem. Mater.* **2014**, *26*, 6185−6192.
(42) Groom, C. R.; Bruno, I. J.; Lightfoot, M. P.; Ward, S. C. The Cambridge Structural Database. *Acta Crystallogr. Sec. B* **2016**, *72*, 171−179.
(43) Landers, J.; Gor, G. Y.; Neimark, A. V. Density functional theory methods for characterization of porous materials. *Colloids Surf. A: Physicochem. Eng. Asp.* **2013**, *437*, 3−32.

https://doi.org/10.1021/acsanm.1c00937
ACS Appl. Nano Mater. 2021, 4, 5531−5540